Journal of Hydroscience and Hydraulic Engineering
Vol. 17, No.1 May, 1999, 117-129

NUMERICAL STUDY OF 2-D INCLINED STARTING PLUMES USING LES

By

Xinya Ying, Juichiro Akiyama and Masaru Ura

Department of Civil Engineering, Faculty of Engineering
Kyushu Institute of Technology, Kitakyushu 804-8550, Japan

SYNOPSIS

The motion of starting plumes moving along an incline is investigated by large eddy simulations (LES). The formulation of the model is based on the filtered two-dimensional Navier-Stokes equations and the conservation of mass. The subgrid-scale turbulent stress is evaluated by the Smagorinsky model. It is found that the model can give a good description of such flow characteristics of the front of inclined starting plumes as the propagation speed, the growth rate of height and length, the entrainment rate and others over a wide range of slope angle ($10° \leqq \theta \leqq 90°$), when the Smagorinsky constant $Cs = 0.06 + 0.1 \sin\theta$ as well as the subgrid turbulent Schmidt number $Scs = 0.4 - 0.3 \sin\theta$. The computational results also provided a good description of the internal flow structure of the front.

INTRODUCTION

When dense fluid is continuously released into a less dense environment, the dense fluid will move along an incline and spread under the action of its own buoyancy force (see Fig.1). The motion of this form is referred to as an inclined starting plume. It consists of the front part characterized by a raised head and the body part characterized by a thinner flow behind the front. The discharges of sediment-laden water and dense wastewater into a reservoir or coastal regions are typical examples of inclined starting plumes.

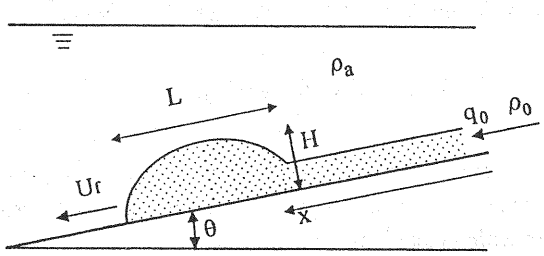

Fig. 1 Definition sketch of an inclined plume

A great deal of experimental and analytical studies on inclined starting plumes has been performed. For example, Britter and Linden (1) have studied experimentally the flow characteristics of inclined starting plumes over a range of slopes $5° \leqq \theta \leqq 90°$ and found the dimensionless front propagation speed as $U_f^* = U_f/(B_0 q_0)^{1/3} = 1.5 \pm 0.2$, where U_f is the front propagation speed; B_0 is the inflow buoyancy force ($= g(\rho_0 - \rho_a)/\rho_a$); g the gravitational acceleration; ρ_0 the density of inflow; ρ_a the density of ambient fluid; q_0 the inflow rate. They also found that the rate of growth of the front height dH/dx and the aspect ratio of height to length of the front H/L are linearly proportional to slope angle θ. Further experimental studies on inclined starting plumes over the same range of slope angles have been performed by Akiyama et al.(2) and more detailed and accurate information on the flows has been obtained. A theoretical model to predict such plume characteristics as front velocity, height and density has been also developed by Akiyama et al. (3), (4).

In the aspect of the numerical simulations of inclined starting plumes, only few studies have been

performed. For example, Michioku et al. (5) used the $k-\varepsilon$ model to simulate the flow on a slope of θ =5.71°, yet only made a few qualitative analyses on the flow characteristics of the front. Cheong and Young (6) numerically investigated two-dimensional inclined plumes produced by a constant discharge of cold water by solving the vorticity equation and heat transport equation.

In this study, the large eddy simulation (LES) is employed to simulate the flow characteristics of the front of inclined starting plumes. The subgrid-scale turbulent stress is evaluated by the Smagorinsky model. It is known that a large range of scales exists in turbulent flows and various scales make different contributions to the Reynolds stress. In addition, large scales can not be always considered as isotropic. These lead the fact that large-scale-averaging approach for turbulent simulation is not always satisfactory. The direct numerical simulations (DNS), in which the whole range scales are computed by using very fine mesh, require considerable computational time and computer memory. Instead, the LES appears to be a promising approach to overcome these difficulties. In the LES only the effect of small scales is modeled, while the large scales are directly computed. Since small scales tend to be more isotropic than the large ones, the modeling of them should be simpler and more universal than the large-scale-averaging approach.

Since Deardorff (7) made his pioneer contribution, the LES has been developed further by Schumann (8), Moin and Kim (9), Horiuti (10), Piomelli et al. (11), Yoshizawa (12), (13), Germano et al. (14) and others. The results obtained by these investigators show that the LES with the Smagorinsky model can yield good predictions for turbulent channel flows, thermal convection and other turbulent flows.

In present work, the operator-split algorithm is used to solve governing equations, that is, the filtered two-dimensional Navier-Stokes equations and the equation of mass conservation. The advection terms in governing equations are solved by the Hermitian interpolated characteristic method (HIC). The values of the Smagorinsky constant Cs and the subgrid turbulent Schmidt number Scs in a range of slope angle ($10° \leqq \theta \leqq 90°$) are determined by detailed comparisons between computational and experimental results.

MODEL FORMULATION

In the LES, the large-scale quantities $F(\vec{r},t)$ (i.e. average values in local space) are defined by convolution of the physical variates $f(\vec{r},t)$ with a filter function $G(\vec{r},\vec{r}')$, where $\vec{r}$ is coordinate in space.

$$F(\vec{r},t)=\int_{\infty} G(\vec{r},\vec{r}')f(\vec{r}',t)d\vec{r}' \tag{1}$$

By applying the grid filter to the two-dimensional incompressible Navier-Stokes equations and the equation of conservation of mass, ignoring Leonard and Cross terms (15), we can obtain the following governing equations.

$$\frac{\partial U_i}{\partial x_i}=0 \tag{2}$$

$$\frac{\partial U_i}{\partial t}+U_j\frac{\partial U_i}{\partial x_j}=-\frac{1}{\rho}\frac{\partial P}{\partial x_i}+\nu\frac{\partial^2 U_i}{\partial x_j^2}+\frac{\partial}{\partial x_j}\left(-\overline{u_i' u_j'}\right)+g_i\frac{\Delta\rho}{\rho} \tag{3}$$

$$\frac{\partial \Delta\rho}{\partial t}+U_i\frac{\partial \Delta\rho}{\partial x_i}=\frac{\partial}{\partial x_i}\left(-\overline{u_i'\,\Delta\rho'}\right) \tag{4}$$

where U_i = large-scale quantities of velocity component in the direction x_i; P = large-scale pressure minus the hydrostatic pressure at reference density ρ_a; ρ = large-scale density; $\Delta\rho$ = density excess ($=\rho-\rho_a$); g_i = i-component of gravitational accelation; $u_i', \Delta\rho'$ = fluctuating velocity and density excess. $\overline{u_i' u_j'}$ =

Reynolds stress. By using eddy viscosity concept, we have

$$-\overline{u_i'u_j'} = \nu_t\left(\frac{\partial U_i}{\partial x_j}+\frac{\partial U_j}{\partial x_i}\right)-\frac{2}{3}k\,\delta_{ij} \tag{5}$$

where ν_t = subgrid scale eddy viscosity; k = turbulent kinetic energy ; δ_{ij} = the Kronecker delta function. The last term in Eq. 5 represents the normal stresses and can be absorbed in the pressure terms of the momentum equations.

In the Smagorinsky model, the eddy viscosity ν_t is obtained by assuming that turbulent energy production and dissipation of subgrid scale eddies are in balance. This leads the following well-known expression

$$\nu_t = (Cs\,\Delta)^2\left|\overline{S}\right| \tag{6}$$

where Δ = filter width, Cs = the Smagorinsky constant, and $\left|\overline{S}\right| = \left(2\overline{S}_{ij}\overline{S}_{ij}\right)^{1/2}$ is the magnitude of large-scale strain rate tensor in which $\overline{S}_{ij}$ is defined by

$$\overline{S}_{ij} = \frac{1}{2}\left(\frac{\partial U_i}{\partial x_j}+\frac{\partial U_j}{\partial x_i}\right) \tag{7}$$

According to Miyake and Kajishima (16), the Smagorinsky constant needs some adjustments from flow to flow and the values vary from 0.07 to 0.27. More specifically, Lilly (17) used Cs=0.23 for homogeneous isotropic turbulence; Deardorff (7) used Cs=0.1 for turbulent channel flow; Piomelli et al. (11) also found the optimum value of Cs to be around 0.1 for turbulent channel flow.

The term $-\overline{u_i'\Delta\rho'}$ in Eq. 4 is generally assumed to be

$$-\overline{u_i'\Delta\rho'} = \frac{\nu_t}{Scs}\frac{\partial\Delta\rho}{\partial x_i} \tag{8}$$

where Scs = the subgrid turbulent Schmidt number and is defined as the ratio of eddy diffusivity of momentum to eddy diffusivity of matter. To the authors' best knowledge, so far the universal expression on the values of Scs has not been available. According to the studies by Reynolds (18), it can be assumed that turbulent Schmidt number bears perfect analogy with turbulent Prandtl number, the ratio of eddy diffusivity of momentum to eddy diffusivity of heat. Concerning subgrid turbulent Prandtl number Prs, Eidson (19) suggests Prs=1/2～1/3.

NUMERICAL SCHEME

In the operator-split algorithm, if the physical variates at $t=n\Delta t$, namely, U_i^n, P^n and $\Delta\rho^n$ are known, U_i^{n+1}, P^{n+1} and $\Delta\rho^{n+1}$ are calculated by the successive application of the following three steps:

1) Advection

$$\frac{\partial U_i}{\partial t}+U_j\frac{\partial U_i}{\partial x_j}=0 \qquad [n\Delta t\le t\le(n+\frac{1}{3})\Delta t] \tag{9}$$

$$\frac{\partial \Delta \rho}{\partial t} + U_j \frac{\partial \Delta \rho}{\partial x_j} = 0 \qquad [n\Delta t \le t \le (n+\frac{1}{2})\Delta t] \tag{10}$$

2) Diffusion

$$\frac{\partial U_i}{\partial t} = \nu \frac{\partial^2 U_i}{\partial x_j^2} + \frac{\partial}{\partial x_j}\left(\nu_t \left(\frac{\partial U_i}{\partial x_j} + \frac{\partial U_j}{\partial x_i} \right) \right) \qquad [(n+\frac{1}{3})\Delta t \le t \le (n+\frac{2}{3})\Delta t] \tag{11}$$

$$\frac{\partial \Delta \rho}{\partial t} = \frac{\partial}{\partial x_j}\left(\frac{\nu_t}{Scs} \frac{\partial \Delta \rho}{\partial x_i} \right) \qquad [(n+\frac{1}{2})\Delta t \le t \le (n+1)\Delta t] \tag{12}$$

3) Pressure

$$\frac{\partial U_i}{\partial x_i} = 0 \tag{13}$$

$$\frac{\partial U_i}{\partial t} = -\frac{1}{\rho}\frac{\partial P}{\partial x_i} + g_i \frac{\Delta \rho}{\rho} \qquad [(n+\frac{2}{3})\Delta t \le t \le (n+1)\Delta t] \tag{14}$$

By using the operator-split algorithm, different steps can be solved separately by the schemes suited for each step. In the advection step, considerable unphysical oscillation and diffusion often occur when such conventional difference methods as first-order upwind , QUICK and Lax-Wendroff scheme are used. To overcome these difficulties, we used the Hermitian interpolated characteristic method (HIC) in the advection step.

The HIC scheme is described in the followings by considering a two-dimensional advection equation

$$\frac{\partial f}{\partial t} + U_1 \frac{\partial f}{\partial x} + U_2 \frac{\partial f}{\partial y} = 0 \tag{15}$$

For Eq. 15, there are characteristic lines determined by

$$\frac{dx}{dt} = U_1 \tag{16}$$

$$\frac{dy}{dt} = U_2 \tag{17}$$

If AB is a characteristic line through node point B and scalar quantity f is transported from A to B during $n\Delta t \le t \le (n+s)\Delta t$, we therefore have

$$f^{n+s}(x_B, y_B) = f^n(x_A, y_A) \tag{18}$$

where s = a parameter used to adjust time step to fit advection step in Eqs. 9 and 10; x_A and y_A can be determined by integrating Eqs. 16 and 17.

By differentiating Eq. 15, we can obtain

$$\frac{\partial f_x}{\partial t} + U_1 \frac{\partial f_x}{\partial x} + U_2 \frac{\partial f_x}{\partial y} + \frac{\partial U_1}{\partial x} f_x + \frac{\partial U_2}{\partial x} f_y = 0 \tag{19}$$

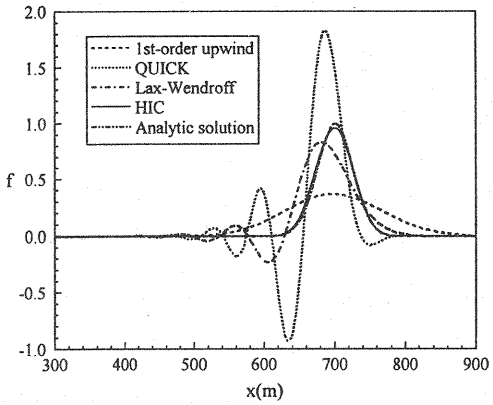

Fig. 2 Comparison of some numerical schemes for 1-D advection problem (t=500 s)

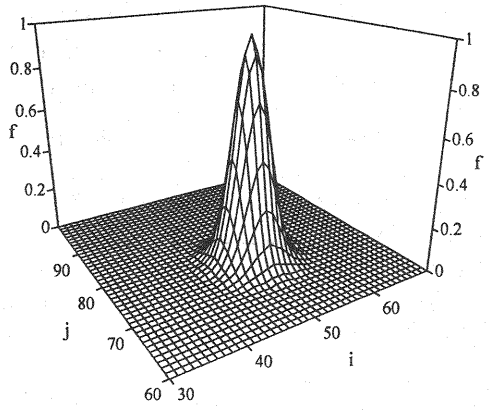

Fig. 3-a Initial distribution for 2-D advection problem

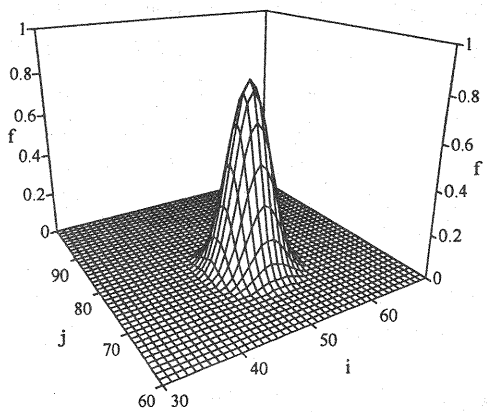

Fig. 3-b Solution by HIC scheme

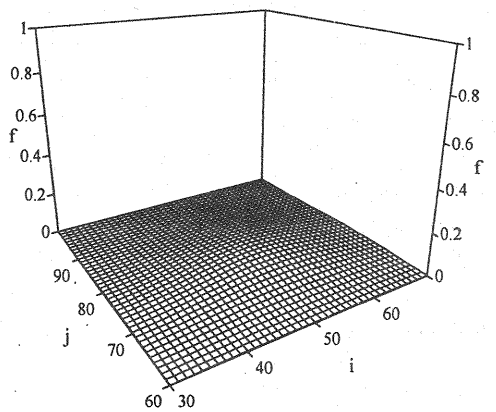

Fig. 3-c Solution by 1st-order upwind scheme

$$\frac{\partial f_y}{\partial t} + U_1 \frac{\partial f_y}{\partial x} + U_2 \frac{\partial f_y}{\partial y} + \frac{\partial U_1}{\partial y} f_x + \frac{\partial U_2}{\partial y} f_y = 0 \qquad (20)$$

where $f_x = \frac{\partial f}{\partial x}$ and $f_y = \frac{\partial f}{\partial y}$. Equation 19 is split into two steps

1st step: $$\frac{\partial f_x}{\partial t} + U_1 \frac{\partial f_x}{\partial x} + U_2 \frac{\partial f_x}{\partial y} = 0 \qquad (21)$$

2nd step: $$\frac{\partial f_x}{\partial t} + \frac{\partial U_1}{\partial x} f_x + \frac{\partial U_2}{\partial x} f_y = 0 \qquad (22)$$

Equation 21 is a pure advection equation on f_x, we therefore have

$$f_x^{n+s}(x_B, y_B) = f_x^n(x_A, y_A) \qquad (23)$$

Finally, $f_x^{n+s}(x_B, y_B)$ is corrected based on Eq. 22 by explicit central difference scheme. $f_y^{n+s}(x_B, y_B)$ is obtained by same approach. In order to improve accuracy, $f^n(x_A, y_A)$, $f_x^n(x_A, y_A)$ and $f_y^n(x_A, y_A)$ are calculated by the two-dimensional Hermitian interpolation.

For diffusion steps, Eqs. 11 and 12 are discretized by central difference scheme. The pressure is obtained by solving the Poisson type equation deduced from the algebraic manipulation of Eqs. 13 and 14.

In what follows, the comparisons between the proposed scheme and the aforementioned conventional schemes are made by advecting a Gaussian profile: $f(x)=\exp(-\frac{(x-x_0)^2}{2\sigma_0^2})$, where $x_0=200\,\text{m}$, $\sigma_0=25\,\text{m}$. The other computational conditions are as follows: velocity $U=1\,\text{m/s}$, space step size $\Delta x=10\,\text{m}$, time step size $\Delta t=2\,\text{s}$ and Courant number $Cr=\Delta tU/\Delta x=0.2$. Figure 2 shows that the HIC scheme yields much better result than other three schemes.

The HIC scheme for two-dimensional advection problems is investigated by advecting a Gaussian hill (Fig.3-a) with initial concentration distribution

$$f(x,y)=\exp(-\frac{(x-x_c)^2+(y-y_c)^2}{2\sigma_0^2})$$

where x_c, y_c = coordinates of initial concentration distribution center. The steady rotational flow field is $U_1=-\omega(y-y_0)$ and $U_2=\omega(x-x_0)$, where ω is an angular velocity in radians/sec and (x_0,y_0) is the axis of rotation. In particular, $x_c=500\,\text{m}$, $y_c=750\,\text{m}$, σ_0=25m, $x_0=500\,\text{m}$, $y_0=500\,\text{m}$, $\omega=2\pi/628$. The computational domain is a square with 100×100 cells. The space step size $\triangle x=\triangle y=10\text{m}$. The time step size $\triangle t=1\text{s}$. Because this is a pure advection problem, the concentration distribution should remain constant throughout the rotation. Therefore we can evaluate the accuracy of a scheme based on its ability to transport the concentration distribution without deformation. The numerical solutions after one revolution (t=628 s) by the HIC scheme and the first-order upwind scheme are shown in Figures 3-b and 3-c, respectively. It is seen from these figures that the result by the HIC scheme has only a small undershooting and is free from numerical oscillation, while the result by the 1st-order upwind scheme is very diffusive.

COMPUTATIONAL RESULTS

The computational conditions for calculating inclined starting plumes are summarized in Table 1. The computational domain is a rectangle. The size of domain is selected depending on the slope angle θ. Grid size is $1\text{cm}\times1\text{cm}$. The time step size ranges from 0.001 s to 0.1 s depending on the slope angle θ and the inflow buoyancy flux B_0q_0.

By comparing such main flow characteristics as dimensionless propagation speed U_f^*, the growth rate of height dH/dx and the aspect ratio of the front H/L between the computational results and the experimental data obtained by Akiyama et al. (2), the optimum value of Cs within a range of $10°\leqq\theta\leqq90°$ is determined as

$$Cs=0.06+0.1\sin\theta \qquad (24)$$

Cs ranges from 0.077 to 0.16 over this range of slope angle and it is consistent with previous studies (16). Similarly, the optimum value of Scs within a range of $10°\leqq\theta\leqq90°$ is determined as

$$Scs=0.4-0.3\sin\theta \qquad (25)$$

Table 1. Computational conditions

$\theta°$	B_0 (cm/s^2)	q_0(cm^2/s)	L_X (cm)	L_Y (cm)
10	9.80	3.34	350	50
20	9.80	2.16	250	60
30	9.80	2.16	250	80
45	9.80	2.02	250	80
60	9.80	2.02	250	100
70	9.80	2.02	250	110
80	9.80	2.00	250	120
90	9.80	2.00	250	120

* L_X and L_Y are length and height of computational domain

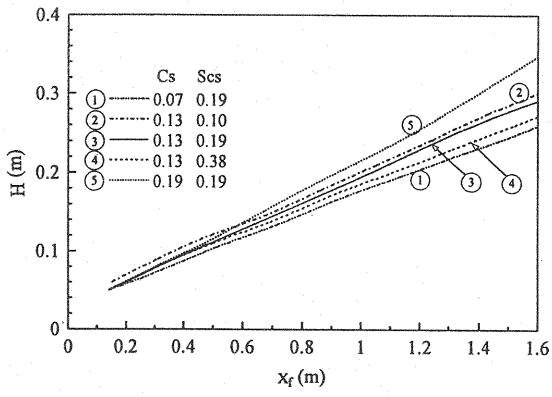

(a)

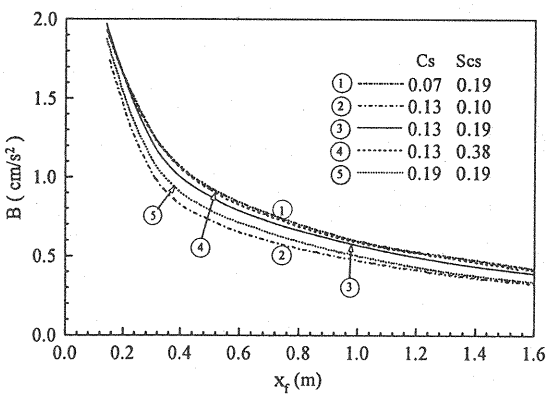

(b)

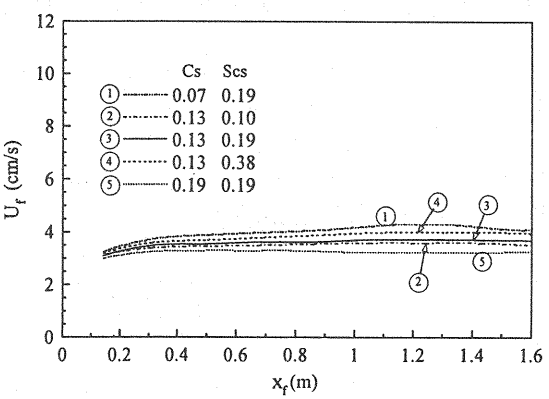

(c)

Fig. 4 Effect of Cs and Scs on H, B and U_f
(θ =45°, B_0=9.8cm/s², q_0=2.02cm²/s)

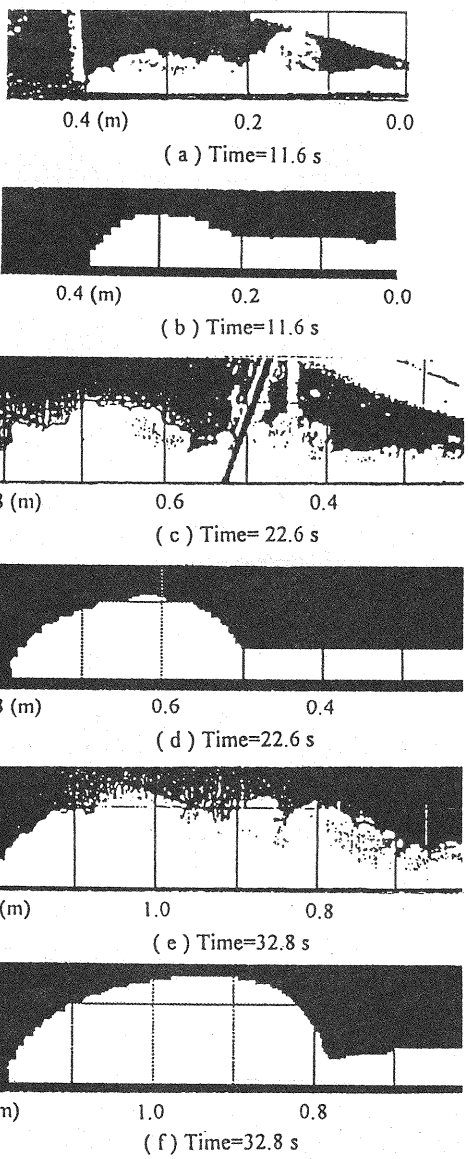

Fig.5 Experimental and computational images of front for θ =20° , b_0=9.8cm/s² , q_0=2.16cm²/s. (a), (c) and (e) are photographs from experiment. (b), (d) and (f) are computational images corresponding to (a), (c) and (e).

The sensitivity analyses of Cs and Scs are presented in Fig.4. Three values of Cs (0.07, 0.13 and 0.19) and Scs (0.10, 0.19 and 0.38) are used in the analyses. The solid line in Fig.4 is the computational results using values of Cs=0.13 and Scs=0.19 that are determined by Eqs. 24 and 25, respectively. Fig.4-a shows that computational results of the height of the front H for Cs=0.19 is about 10% larger than that for Cs=0.13 and computed H for Cs=0.07 is about 10% smaller than that for Cs=0.13, when Scs has the same value of 0.19. Fig.4-a also indicates that computed H is sensitive to Scs. From Figs.4-b and 4-c, we found that computational results of average buoyancy B and front propagation speed U_f have smaller values when larger value of Cs and smaller value of Scs are used.

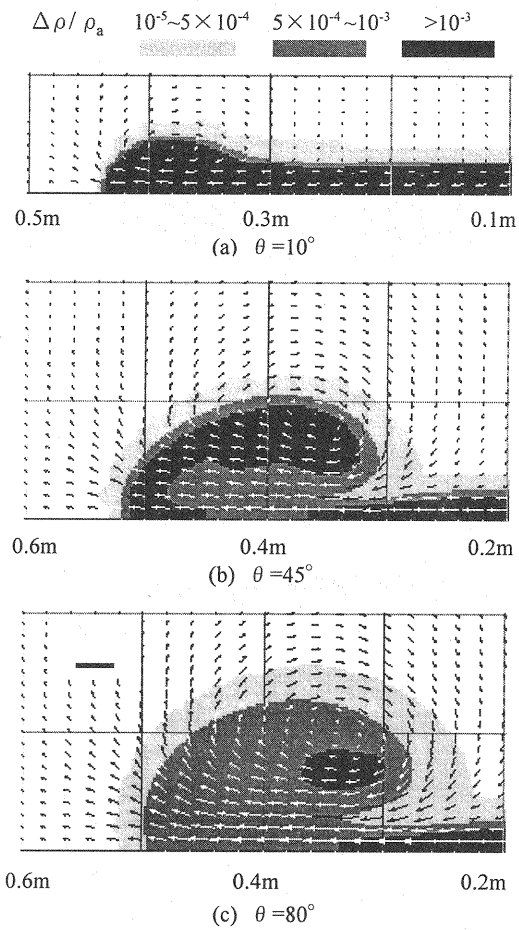

Fig. 6 Flow and density excess pattern
(B_0 =9.8 cm/s², q_0 =2.0 cm²/s)

In what follows, the computational results by using the above optimum values of Cs and Scs are compared with experimental results.

Comparisons between Experimental and Computational Images

Figure 5 shows the comparisons of experimental and computational image of the flow at the slope angle θ =20°. In the computational results, the region of plume is defined by $\Delta \rho / \rho_a \geq 10^{-5}$. They are in agreement in shape, size and front velocity. In the experiment, it is observed that the flow at the wake of the front is quite unstable and part of dense clouds is left behind when slope angle θ is less than 20°. This phenomenon does not appear in the computation and it leads some difference between the experimental images and the computational images.

Flow and Density Excess Patterns

Figure 6 shows computed flow and density excess patterns of the front for different θ at time=16 s. It shows that the front approximately keep the shape of half-ellipse as reported in previous experimental studies (1), (2), and its size increases with θ. The flow pattern at the front is characterized by a large vortex motion centered near the top of the front. The vortex motion becomes stronger as θ increases. By comparing these figures, we can find that the entertainment of ambient fluid at the rear of the front becomes stronger as θ increases. It is also observed that the density excess fields for small slope angles are different from large slope angles. In the cases of such large slope angle as θ = 45° and 80°, a peak of density excess appears at the place little lower than the center of the vortex motion, due to the stronger entrainment of less dense fluid from the back side of the front. On the other hand, for the case of θ = 10° the maximum of density excess always appears near the bottom.

U_f, H and H/L as Functions of x_f

An example of computational result of the front propagation speed U_f, the height of the front H and the aspect ratio of the front H/L is plotted against the distance from inlet to the front position x_f in Figs. 7, 8 and 9. Symbols shown in the figures are experimental results obtained by Akiyama et al. (2). It is seen that the computational and experimental results are in good agreement. These figures also show that the values of U_f and H/L are nearly constant, and H increases linearly as x_f increases. These results are consistent with experimental findings (1), (2). The same results are obtained for the flow at different slope angles.

U_f^*, dH/dx and H/L as Functions of $B_0 q_0$

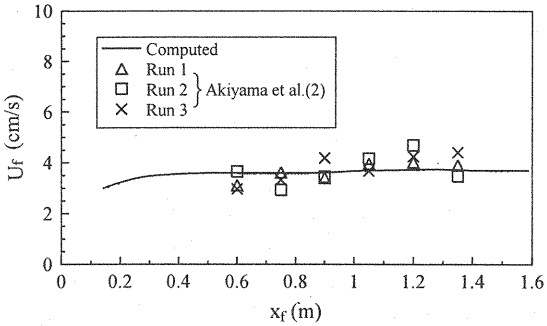

Fig. 7 U_f as a function of distance
($\theta = 45°$, $B_0 = 9.8$ cm/s^2, $q_0 = 2.02$ cm^2/s)

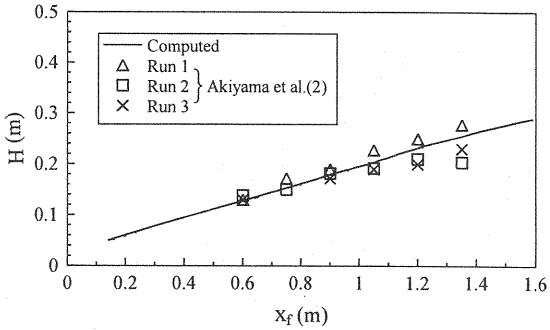

Fig. 8 H as a function of distance
($\theta = 45°$, $B_0 = 9.8$cm/s^2, $q_0 = 2.02$cm^2/s)

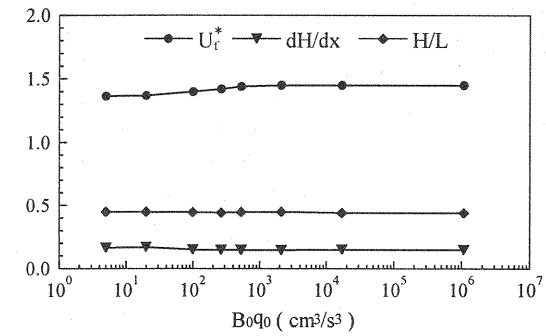

Fig. 9 H/L as a function of distance
($\theta = 45°$, $B_0 = 9.8$ cm/s^2, $q_0 = 2.02$ cm^2/s)

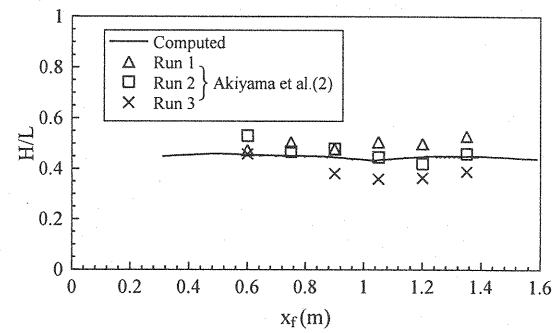

Fig. 10 U^*_f, dH/dx and H/L as a function of inflow buoyancy flux B_0q_0 ($\theta = 45°$)

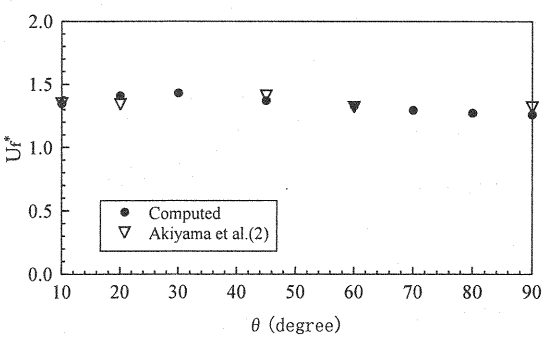

Fig. 11 U^*_f as a function of θ
(B_0 and q_0 are shown in Table 1)

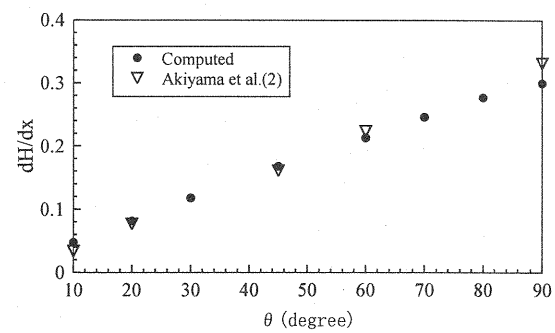

Fig. 12 dH/dx as a function of θ
(B_0 and q_0 are shown in Table 1)

Britter & Linden (1) and Akiyama et al. (2) have experimentally investigated the effect of inflow buoyancy flux B_0q_0 on the front of inclined starting plumes and found U^*_f, dH/dx and H/L are almost independent of B_0q_0 over a range of 2.5 cm^3/s^3 $\leq B_0q_0 \leq$ 250 cm^3/s^3. In order to confirm this experimental finding, the computed U^*_f, dH/dx and H/L at slope angle $\theta = 45°$ are plotted against B_0q_0 in Fig. 10. It shows that no evident dependence of U^*_f, dH/dx and H/L on B_0q_0 is found over a very wide range of 4.95 cm^3/s^3 $\leq B_0q_0 \leq 1.08 \times 10^6$ cm^3/s^3. The constancy of U^*_f, dH/dx and H/L against B_0q_0 is also observed at other slope angles.

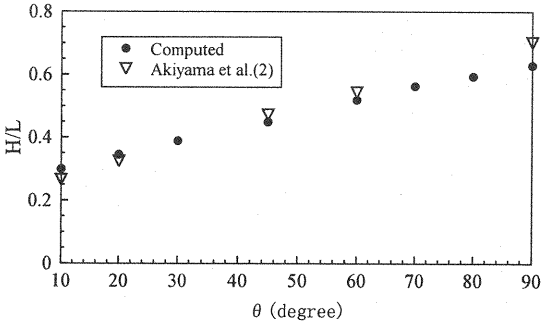

Fig. 13 H/L as a function of θ
(B_0 and q_0 are shown in Table 1)

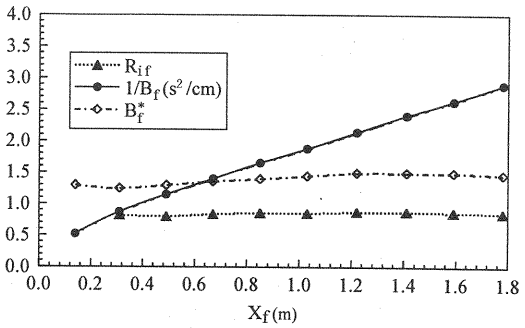

Fig. 14 R_{if}, B_f and B_f^* as functions of distance
($\theta = 45°$, $B_0 = 9.8 cm/s^2$, $q_0 = 2.02 cm^2/s$)

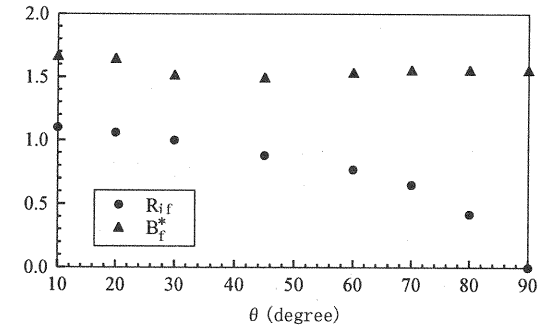

Fig. 15 R_{if} and B_f^* as functions of θ
(B_0 and q_0 are shown in Table 1)

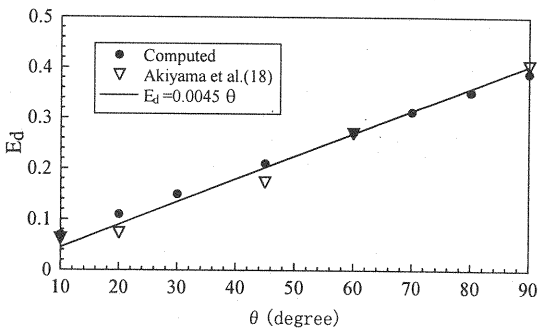

Fig. 16 E_d as a function of θ
(B_0 and q_0 are shown in Table 1)

U_f^*, dH/dx and H/L as Functions of θ

Computed U_f^*, dH/dx and H/L as well as experimental results obtained by Akiyama et al. (2) are plotted against θ in Figs. 11, 12 and 13, respectively. Figure 11 shows that the values of U_f^* are nearly constant and around 1.35 over a range of $10° \leq \theta \leq 90°$, which is very close to the value of 1.34 ± 0.03 determined experimentally for $5° \leqq \theta \leqq 90°$ by Akiyama et al. (2). As shown in Figs. 12, the computed dH/dx increases linearly with θ from 0.048 at $\theta = 10°$ to a maximum of 0.3 at $\theta = 90°$. This is in good agreement with the experimental results, which increases from 0.034 at $\theta = 10°$ to 0.332 at $\theta = 90°$. Figure 13 shows that computed H/L increases linearly with θ and no considerable difference is found between the computational and the experimental results.

Overall Richardson Number and Buoyancy Force

In Fig. 14, the computed values of the overall Richardson number $R_{if} = \dfrac{(\Delta \rho_f / \rho_0) g H \cos\theta}{U_{fc}^2}$, averaged buoyancy force at the front $B_f = (\Delta \rho_f / \rho_0) g$ and dimensionless buoyancy force $B_f^* = \dfrac{(\Delta \rho_f / \rho_0) g H}{(B_0 q_0)^{2/3}}$ for the case of $\theta = 45°$ are plotted against x_f, where U_{fc} is mass center velocity of the front. It is found that R_{if} and B_f^* are almost constant and $1/B_f$ is almost linearly proportional to x_f. These results are consistent with experimental and theoretical results reported by Akiyama et al. (3), (4). The computed R_{if} and B_f^* are

plotted against θ in Fig.15. It is found that the values of R_{if} decrease with θ and the values of B_f^* are around 1.55 over a range of $10° \leq \theta \leq 90°$.

Entrainment Coefficient

The entrainment coefficient is defined as $E_d = \frac{q_e}{LU_f}$, where q_e is the rate of entrainment of ambient fluid into the front part ($= dA/dt - q_i$), and A is the area of the front part; q_i is flow rate from the body part into the front part and is calculated by $q_i = \int_0^{H_b} [U_1(y) - U_b]dy$, in which H_b is the height of the body part at the section just behind the front, $U_1(y)$ is the velocity component in x-direction at the section just behind the front and U_b is the propagation speed of the back side of the front.

Experimental studies by Akiyama et al. (20) have shown that E_d increases linearly with θ and an empirical equation E_d=0.0045 θ is obtained based on a large number of experimental data for $5° \leqq \theta \leqq 90°$. In Fig. 16, the computed E_d along with the experimental results is plotted against θ. It is seen that the computed values of E_d fit well with the empirical formula given by Akiyama et al.(20).

CONCLUSIONS

In simulating an inclined starting plume, excessive accuracy is required in solving the equation of mass conservation, because such density current as an inclined starting plume is essentially induced by buoyancy force. The computational results show that the model overcomes the difficulties by using the HIC scheme in solving the governing equations.

Through comparisons between the computational results and the experimental results obtained by Akiyama et al. (2), (3), the optimum values of Cs and Scs for inclined starting plumes over a range of slope angle ($10° \leqq \theta \leqq 90°$) are determined as Eqs. 24 and 25, respectively. The model with the optimum values of Cs and Scs gives a good description of the front of inclined starting plumes over a wide range of slope ($10° \leqq \theta \leqq 90°$).

REFERENCES

1. Britter, R.E. and P.F. Linden : The motion of the front of a gravity current traveling down an incline, J. Fluid Mech., Vol.99, pp.531-545, 1980.
2. Akiyama, J., M. Ura and K. Sakamoto : Flow characteristics and entrainment of two-dimensional starting plumes traveling down slope, J. of Hydroscience and Hydraulic Engineering, Vol.12, No.2, pp.1-16, 1994.
3. Akiyama, J., M. Ura and S. Wongsa : Unsteady numerical model of two-dimensional starting plumes traveling down slope, J. of Hydroscience and Hydraulic Engineering, Vol.12, No.2, pp.17-30, 1994.
4. Akiyama, J., M. Ura and W. Wang : Physical-based numerical model of inclined starting plumes, J. of Hydraulic Engineering, ASCE, Vol.120, No.10, pp.1139-1158, 1994.
5. Michioku, K., Y. Fujikawa and H. Fuji : Analysis on buoyancy inflow behaviors in reservoir, Proceedings of Hydraulic Engineering, JSCE, Vol.40, pp.561-566, 1996, (in Japanese).
6. Cheong, H.B. and Y.H. Han : Numerical study of two-dimensional gravity currents on a slope, Journal of Oceanography, Vol.53, pp.179-192, 1997
7. Deardorff, J.W. : A numerical study of three-dimensional channel flow at larger Reynods numbers, J. Fluid Mech., Vol.41, pp.453-480, 1970.
8. Schumann, U. : Subgrid scale model for finite difference simulations of turbulent flows in plane channels and annuli, J. Comp. Phys., Vol.18, pp.376-404, 1975.
9. Moin, P. and J. Kim : Numerical investigation of turbulent channel flow, J. Fluid Mech., Vol.118, pp.341-377, 1982.

10. Horiuti, K. : Large eddy simulation of turbulent channel flow by one-equation modeling, J. of the Physical Society of Japan, Vol.54, No.8, pp.2855-2865, 1985.
11. Piomelli, U., P. Moin and J.H. Ferziger : Model consisitency in large eddy simulation of turbulent channel flows, Phys. Fluids, Vol.31, pp.1884-1891, 1982.
12. Yoshizawa, A. : Subgrid-scale modeling with a variable length scale, Phys. Fluids A 1 (7), pp.1293-1295, 1989.
13. Yoshizawa, A. : Eddy-viscosity-type subgrid-scale model with a variable Smagorinsky coefficient and its relationship with the one-equation model in large eddy simulation, Phys. Fluids A 3 (8), pp.2007-2009, 1991.
14. Germano, M., U. Piomelli and W.H. Cabot : A dynamic subgrid-scale eddy viscosity model, Phys. Fluids A 3 (7), pp.1760-1765, 1991.
15. Yasuhara, M. and J. Daiguu : Computational fluid dynamics, Press of Tokyo University, 1993, (in Japanese)
16. Miyake, Y. and T. Kajishima : Numerical simulation of turbulent flows, Proceedings of JSME (B), JSME, Vol.53, No.491, pp.1869-1877, 1987, (in Japanese)
17. Lilly, D.K. : On the application of the eddy viscosity concept in the inertial sub-range of turbulence, NCAR Manuscript No.123, National Center for Atmospheric Research, 1966.
18. Reynolds, A.J. : The prediction of turbulent Prandtl and Schmidt numbers, Int. J. Heat Mass Transfer, Vol.18, pp.1055-1069, 1975.
19. Eidson, T.M. : Numerical simulation of the Rayleigh-Benard problem using subgrid modeling, J. Fluid Mech., Vol.158, pp.245-268, 1985.
20. Akiyama, J., M. Ura, S. Saito and N. Tomioka : Entrainment coefficients for gravity currents on inclines, Journal of Japan Society of Fluid Mechanics, Vol.16, pp.149-161, 1997.

APPENDIX – NOTATION

The following symbols are used in this paper:

A	=	area of front part;
B_0	=	buoyancy force of inflow;
B^*_f	=	dimensionless averaged buoyancy force of front part;
Cr	=	Courant number ;
Cs	=	Smagorinsky constant ;
E_d	=	entrainment coefficient for front part;
g	=	acceleration of gravity;
H	=	height of front part;
L	=	length of front part;
Lx, Ly	=	length of computational domain in x-direction and in y-direction respectively;
P	=	pressure;
Prs	=	subgrid turbulent Prandtl number;
q_0	=	flow rate of inflow;
q_e	=	entrainment flow rate of ambient fluid into front part ;

q_i = flow rate from body part into front part;

R_{if} = overall Richardson number of front part;

Scs = subgrid turbulent Schmidt number;

t = time;

U_i = large-scale quantities of velocity component in x-direction (i=1) and y-direction (i=2);

U_f = front propagation speed;

U_{fc} = mass center velocity of the front;

U^*_f = dimensionless front propagation speed;

x, y = longitudinal coordinate and transverse coordinate;

x_f = distance from inlet to front position;

Δt = time step size;

$\Delta x, \Delta y$ = space step size in x-direction and y-direction;

$\Delta \rho$ = density excess;

$\Delta \rho_f$ = averaged density excess of front part;

ν_t = eddy viscosity;

θ = slope angle; and

ρ, ρ_0, ρ_a = density, density of inflow and density of ambient fluid respectively.

(Received August 24, 1998 ; revised October 14, 1998)